Supercapacitance behavior of porous oxide layer grown on 302 type stainless steel substrate

Biplab Sarma [a], York R. Smith [a], Abraham L. Jurovitzki [a], Rupashree S. Ray [a], Swomitra K. Mohanty [b], Mano Misra [a,b,*]

[a] Metallurgical Engineering, University of Utah, Salt Lake City, UT 84112, USA
[b] Chemical Engineering, University of Utah, Salt Lake City, UT 84112, USA

HIGHLIGHTS

► Synthesis of porous oxide layer on 302 type stainless steel substrate by electrochemical anodization method.
► Variations of oxide layer morphology based on the anodization current density and time.
► Specific electrochemical capacitance of as high as 112 mF cm^{-2} at galvanostatic charge–discharge current density of 1 mA cm^{-2}.
► More than 60% capacitance retention even after 500 cycles of continuous charge–discharge.

ARTICLE INFO

ABSTRACT

Nano-porous oxide layers on the surface of 302-type stainless steel were synthesized by galvanostatic anodization process carried out at two current densities, 7 and 15 mA cm^{-2} for the time periods of 15 and 30 min. A relatively thinner ($\sim$300 nm) and compact oxide layer formed when anodization was performed at a current density of 7 mA cm^{-2}. However, with increase in anodization current density, the oxide layer not only grew thicker but also changed in morphology. It was found to be about 0.7 and 1.2 μm after 15 and 30 minutes of anodization at 15 mA cm^{-2}, respectively. The XRD analysis of the oxide layer suggested the formation of hematite ($(Fe, Cr)_2O_3$) and spinel ($(Ni, Cr, Fe)_3O_4$) phases. The cyclic voltammetry and galvanostatic charge-discharge studies (1 M Li_2SO_4) suggested that the nature of the capacitance of the anodized stainless steel electrodes were of predominantly electric double layer (EDL) type together with some pseudocapacitance like behavior. The specific capacitance obtained was higher for the sample anodized at higher current density (15 mA cm^{-2}) than that of the sample anodized at lower current density (7 mA cm^{-2}). The results were also complimented by electrochemical impedance spectroscopic (EIS) analysis.

1. Introduction

Electrochemical capacitors, also known as supercapacitor or pseudocapacitors are characterized by high reversible power density and long cycle life [1,2]. Based on the charge storage mechanism, the electrochemical capacitors are divided into two broad groups: (i) non-faradic electric double layer (EDL) capacitor and (ii) redox capacitor (or pseudocapacitors) [1]. In the former case, the non-faradic separation of charges at the electrode/electrolyte interface

decides the charge storage capacity of the material while for the later case, the fast and reversible faradic reactions that occur in the electrode/electrolyte interface decides the storage capacity. Generally, materials with high porosity and large surface area are desired as the active electrode for electrochemical capacitance application. Previously, activated carbon and carbon aerogels have been suggested as electrode materials; however, rapid degradations have made them inferior choices [3,4]. Further research demonstrated various other potential candidates especially, transition metal oxides/hydroxide based materials as supercapacitors. Among them, Ru [5], Mn [5,6], Ni [4,7], Co [8] were the most commonly studied. However, not as much attention has been given to evaluate some other transition metal oxides, such as iron oxide and/or iron based alloy oxide materials for such application. Few of the studies

indicated that the capacitance behavior observed in iron oxides (α-Fe_2O_3 and Fe_3O_4) is comparable to those obtained in other transition metal oxide capacitors [9]. Furthermore, it was also observed that compared to conventional micro size, nano scale oxide morphologies (nano-size grains, nanotubular array, nanowires, nanorods, etc) of the iron oxides imparted relatively higher capacitance [9]. This is partly because of their higher surface area and more reaction sites [1] facilitating enhanced charge storage and rapid redox reactions. Various preparation methods such as sol–gel process, chemical precipitation, thermal decomposition, hydrothermal, template-based, electrochemical anodization etc. have been adapted to synthesize nano-size iron oxide electrode materials [10]. However, among them, electrochemical anodization has proven to be one of the easily adoptable and facile synthesis methods to form oxide layers because of its low cost and ease of use [9,11–14]. Based on the process parameters, such as anodization potential, temperature, electrolyte composition and prior metal substrate conditions, several nano-shaped morphologies ranging from porous, tubular to hierarchical/hybrid structures can be synthesized [15]. In fact, numerous studies involving the formation of nanoporous oxide surface layer on various valve metals (Al, Ti, Hf, Zr, Nd, W) has also been conducted for various applications [16–26].

Recent studies demonstrated that nano-porous oxide layer can also be grown on various types of stainless steel substrates by electrochemical anodization process [27–29]. For example, anodization of 304 [27,28] and 316 type [29] stainless steel substrates resulted in the formation of porous oxide layers through suitable adjustment of the electrolyte composition. The oxide layer formed on stainless steel substrate are rather different than those grown on pure iron [9,11–14] because in the former case, the layer is actually a mixture of Fe, Cr and Ni oxides [29]. The electrochemical capacitance behavior of the oxide layer grown on stainless steel has not been studied to the best of the author's knowledge. It has been suggested that in the case of pure iron oxides, the electrochemical capacitance is partly from the EDL and partly through the redox reactions depending on the electrolyte used [9]. However, due to the presence of the oxides of Ni and Cr along with that of Fe, the oxide layer of stainless steel may result in additional faradic redox reactions which could potentially contribute toward the electrochemical capacitance. Oxides of transition metals such as Ni and Cr generally show very good electrochemical capacitance [1,30]. Therefore, in this study, we have conducted galvanostatic anodization on 302 type stainless steel to study the evolution of porous oxide layer and subsequently the effect of these layers on supercapacitance behavior of the electrode material. It has also been demonstrated that the anodized stainless steel can be used as supercapacitor owing to its high specific capacitance and high degree of capacitance retention after long charge–discharge operations.

2. Experimental procedure

Stainless steel of type 302 with nominal composition (in wt.%), C: 0.15, Cr: 17–19, Ni: 8–10, Mn: <2, Si: <1, S: <0.03, P: <0.045, balance Fe, was used as the base material. Prior to anodization, coupons of material (10 mm × 10 mm × 0.07 mm) were extracted and polished with emery paper. The polished samples were ultrasonically cleaned for 15 min in a solution containing 50/50 vol% of acetone and isopropyl alcohol. Anodization of the cleaned samples was performed galvanostatically at room temperature in a fluorinated solution of ethylene glycol containing 0.1 M NH_4F and 0.1 M H_2O. Two different current densities, 7 and 15 mA cm^{-2} and various time periods of 15 till 30 min were employed during anodization. Anodized samples were cleaned by sonication for ~3 s in DI water followed by drying in air. Annealing was carried out in a laboratory

scale box furnace at 500 °C for 2 h in air atmosphere. For comparative study with that of the anodized samples, one sample was cleaned and annealed in similar condition without any anodization.

The morphologies of the oxide layers formed by anodization were examined with scanning electron microscope (Hitachi, S-4800). The crystal phases and the composition of the materials were determined by X-ray diffraction (XRD) and energy dispersed X-ray spectroscopy (EDS), respectively. The XRD analysis of the samples was carried out using SIEMENS D5000 diffractometer with copper K-α radiation. The diffraction tests were done by 2θ to 2θ scan from 10° to 80°. EDS analysis was done using oxford system (X-Max) attached to the Hitachi S-4800 SEM system.
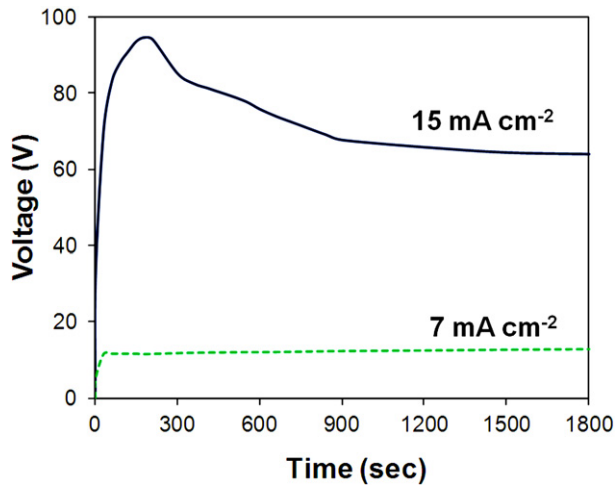
The electrochemical tests, cyclic voltammetry, galvanostatic charge–discharge and electrochemical impedance spectroscopy (EIS) were conducted in a three-electrode configuration with anodized stainless steel substrate as the anode, a platinum flag as the cathode, and Ag/AgCl (3 M KCl) as reference electrode. The electrolyte was an aqueous solution of 1.0 M Li_2SO_4 (pH ~8). A computer-controlled potentiostat (Gamry 600) was used to control the potential and current during all electrochemical experiments. For the EIS studies, a Partstat 4000 EIS analyzer (Princeton Applied Research) and ZSimpWin software was used to carry out the experiments and analyze the data. EIS data was collected at open-circuit potential (OCP) vs. Ag/AgCl with an AC voltage amplitude of 10 mV and recorded within the frequency range of 0.01–10,000 Hz.
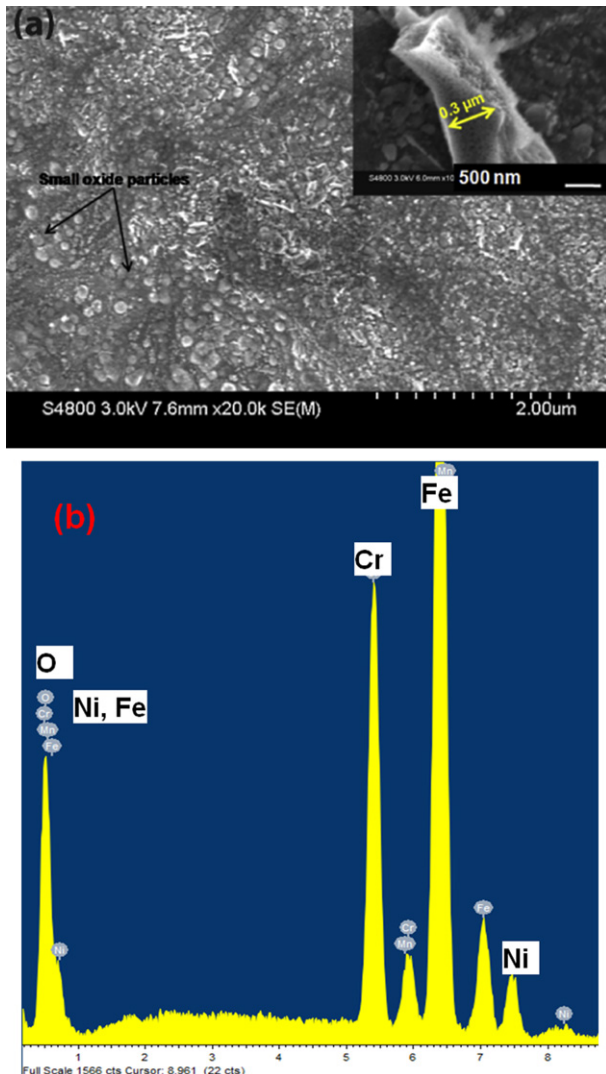
3. Results and discussion

3.1. Synthesis, morphology and crystal structures of oxide phases

The voltage–time responses during galvanostatic anodization of the stainless steel samples at current densities of 7 and 15 mA cm^{-2} are shown in Fig. 1. At 7 mA cm^{-2}, the formation voltage quickly surged to about 11 V in 30 s of the commencement of anodization. The further fluctuations in the voltage were very small reaching a steady state value of 12.8 V for rest of the duration of anodization. On the other hand, a steep increase in voltage was observed when anodization was carried out at 15 mA cm^{-2}. The voltage rose to 94 V after 200 s followed by a gradual decrease to a steady state value of ~65 V after 900 s. The surge and equilibration of the voltage during anodization plays an important role in the morphology and thickness development of the oxide layer as will be explained in the following discussions.
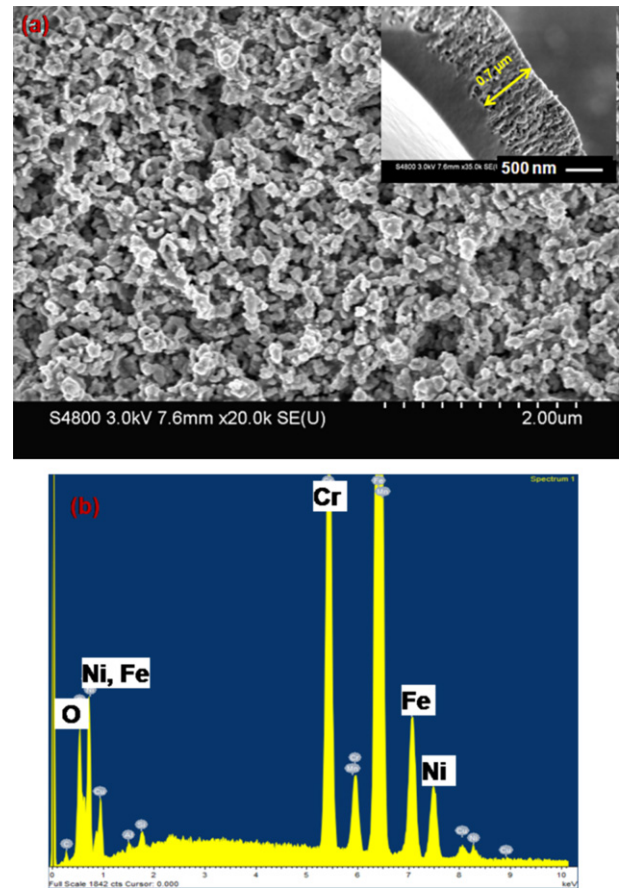
The morphologies of the oxide layers formed on the stainless steel substrates during anodization are shown in Figs. 2–4. Fig. 2a shows SEM image of the top surface of the oxide layer obtained after 30 min of anodization at 7 mA cm^{-2}. The corresponding EDS profile is shown in Fig. 2b. The layer appears to be homogenous, compact, and dense with dispersed nano meter size oxide particles in the range of 25–50 nm (Fig. 2). The thickness of the oxide layer was rather small (300 nm) as illustrated in the inset micrograph of Fig. 2a. The formation of thin layer may be because of the small steady state voltage (~13 V) observed during anodization (Fig. 1). However, with increase in the anodization current density, the morphology and thickness of the oxide layers changed drastically. Fig. 3(a and b) shows the top view of the oxide layer and the corresponding EDS spectrum for the sample anodized at 15 mA cm^{-2} for 15 min. The layer appears to be highly porous with nano size dendritic structures inter-tangled uniformly throughout the entire surface. The EDS spectrum also shows the presence of well-defined oxygen peak along with the metal constituents of the stainless steel alloy. The thickness of the porous layer is about 700 nm (inset in Fig. 3a), which is nearly 2.3 times thicker than that of the layer formed at current density of 7 mA cm^{-2}. Close

examination of the structure of the oxide phase suggests that the dendrites are about 50 nm in width and 150−200 nm in length. It was interesting to note that upon increase in the anodization time, various other morphologies evolved. The nano-dendritic structures seemed to have become foamy and porous in nature when the time was increased to 20 min (Fig. 4b). Further increase in time to 25 min, the foamy layer agglomerated into rectangular shaped particulate as illustrated in the image in Fig. 4c. Finally, the rectangular shaped particulates agglomerated into spherical particles with the increase in anodization time to 30 min as shown in Fig. 4d. Generally, the mechanism of growth of the porous anodic oxide layer on stainless steel substrate is rather complex [28,31]. Some of the elements of the alloy, such as Ni, Co etc., do not resist the etching process by the fluoride ions of the anodization electrolyte [31]. However, they are neither very stable in the electrolyte because of the presence of highly corrosive HF. In one of these studies [31] it was reported that during anodization, "field assisted chemical dissolution" of less stable elements (Ni, Co) occurs leading to the deformation of the porous oxide layer. Such deformation can result in the formation of various morphological changes depending on the anodization potential, current as well as time [31]. It appears that such mechanism of morphology transition can be a primary cause of various shapes of oxide layers obtained in this study with changing anodization time. For a better view, the top surface of the oxide layer formed after 30 min of anodization at 15 mA cm^{-2} resembling leaflet like structure with closely packed oxide particles is shown in Fig. 4e. The compact arrangement of the particles in the thickness direction
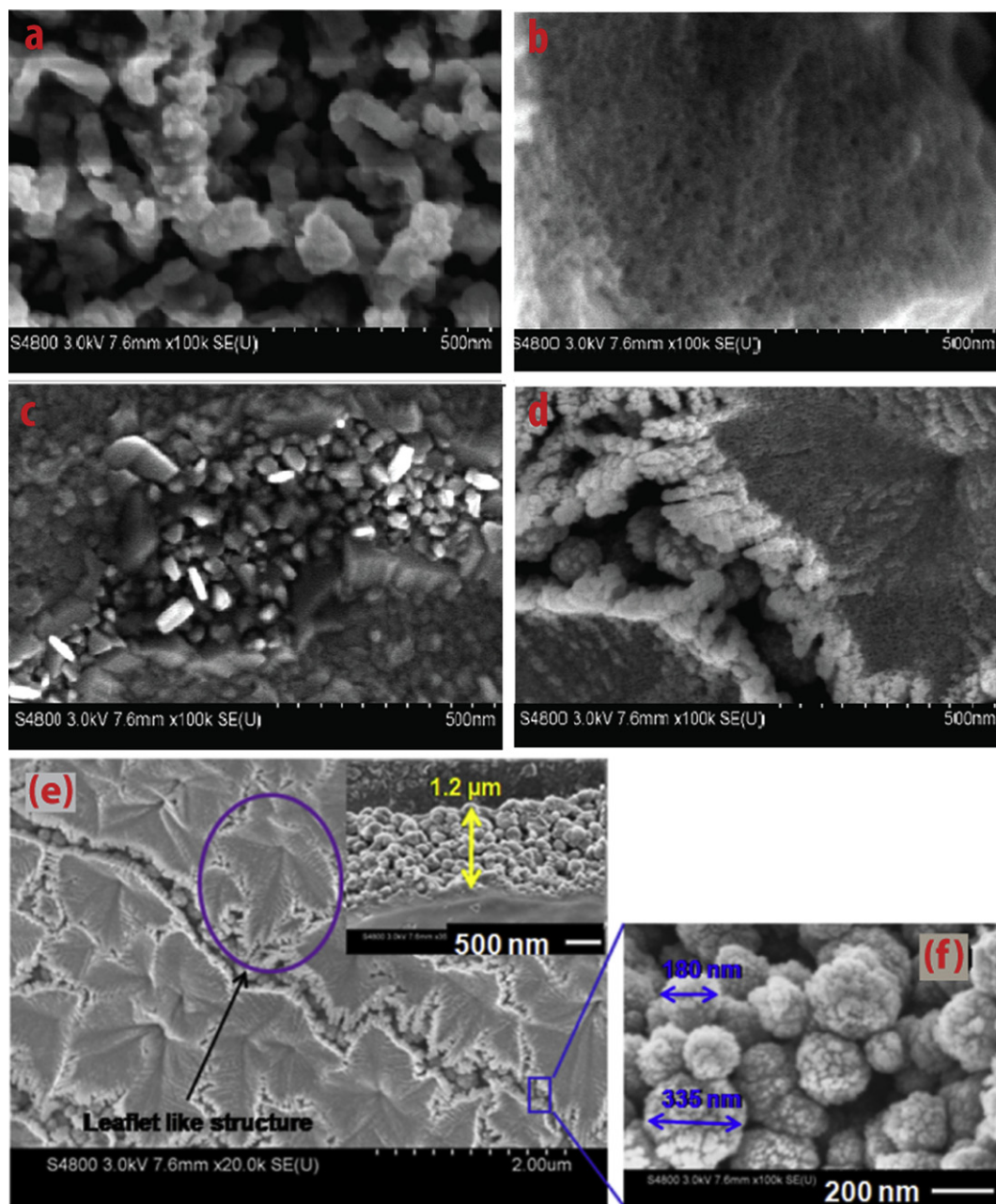
Fig. 4. Higher magnification images of (a) nano-dendritic, (b) foamy, (c) rectangular, and (d) spherical shapes of oxide layers obtained after 15, 20, 25, and 30 min of anodization at current density of 15 mA cm^{-2}, (e) Lower magnification image of the sample obtained after 30 min of anodization at the same current density showing the leaflet morphology (inset showing the thickness of the oxide layer), (f) High magnification image of the spherical oxide particles. The spherical particles appeared to have formed by loose agglomeration of even finer particles.

can also be seen in the inset micrograph of Fig. 4e. The thickness of the oxide layer increased to 1.2 μm after 30 min compared to that of 0.7 μm that formed after 15 min of anodization (inset in Fig. 3a). The typical size range for the spherical particles is in between 150 and 350 nm (Fig. 4f). It is of interest to note that not much significant change in the morphology of the oxide layer was observed in the as anodized condition (without anneal). As a representative, the morphology of the sample obtained after anodization at 15 mA cm^{-2} for 15 min is shown in Fig. 5. The nano-dendritic, inter-tangled features of the oxide layer are quite similar to those obtained in the annealed sample (Fig. 3a). However, the electrochemical properties of such layers suffer significantly compared to their annealed counterpart as will be discussed in the later section.

The surface morphology of the just annealed (500 °C/2 h) sample was also examined microscopically to compare and contrast its oxide layer with those obtained in the anodized samples. The sample was annealed without any anodization, however the annealing temperature and time were kept the same as that of the anodized samples. Fig. 6(a) shows the SEM image of the oxide layer formed on the stainless steel substrate after the annealing process. The EDS profile shown in Fig. 6b, pertaining to the oxide layer confirms the presence of oxygen in the layer. The compactness and uniformity of the oxide layer are comparable to that of the layer formed during anodization at 7 mA cm^{-2} (Fig. 2). However, there exist some salient features about this layer in terms of the morphology of the oxide phase. While the presence of small-scale oxide particles are evident (shown in the Fig. 6a and in the inset
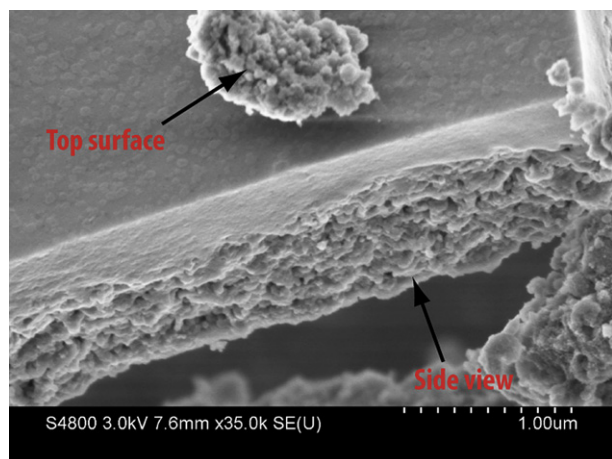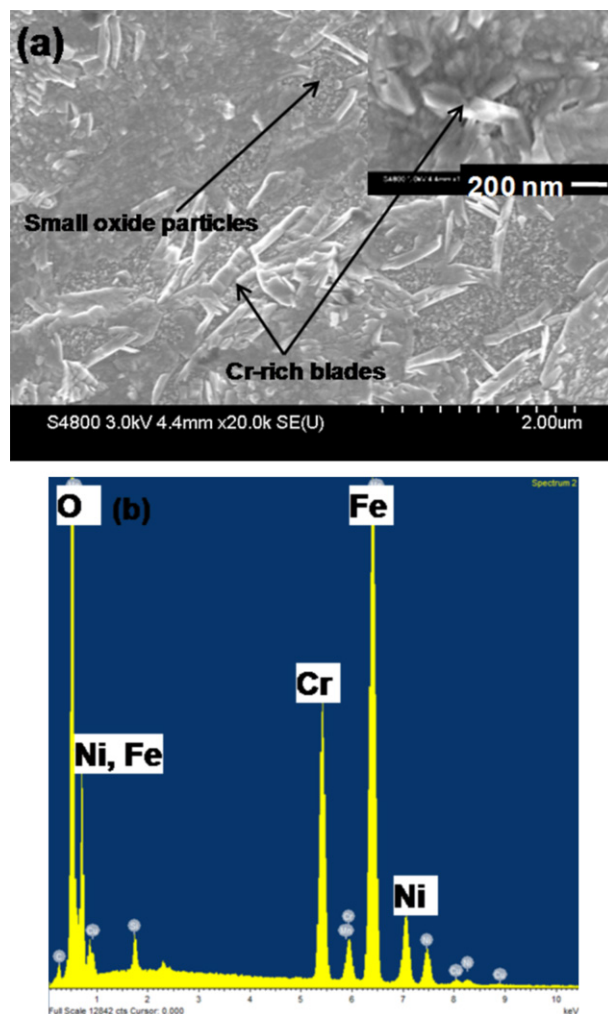
Fig. 5. Morphology of the as-anodized oxide layer formed after 15 min of anodization at 15 mA cm^{-2}.

Fig. 6. (a) Morphology of oxide layer formed during thermal oxidation of 302 type stainless steel at 500 °C for 2 h (b) EDS spectrum of the entire surface.

micrograph), some elongated lathe shaped oxide grains are also visible in the thermally grown oxide layer. The typical width of these lathes is about 75−100 nm, while length is in the range of 200−300 nm. The formation of such lathe was also observed in 316 type stainless steel upon thermal oxidation at 350 °C [32]. Termed as *Cr-rich blade*, these lathes were enriched with Cr content due to the outward diffusion of Cr from the base metal through the oxide layers at elevated temperature. As the level of Cr content in 316 and 302 type stainless steels are comparable, the formation of these blades has also been observed in this case.

Fig. 7 shows the XRD profiles of the oxide layers formed after anodization for 30 min at 7 mA cm^{-2} and 15 min at 15 mA cm^{-2}. The characteristic peaks suggested that the oxide layers are composed of mainly two phases, hematite and spinel in both anodization conditions. It was envisaged that the oxide phases (hematite and spinel) that forms on the surface of stainless steel are generally non-stoichiometric in compositions [33−35]. A compositional analysis study carried out on the oxide layers of 304 type stainless steel revealed the possible formulation of the composition for the hematite phase as $(Fe, Cr)_2O_3$ and spinel as $(Ni, Cr, Fe)_3O_4$ [33]. In our study, the relative peak intensities of the oxide phases appear to be close to each other, suggesting that the oxide layer is enriched with Cr and Ni along with Fe. Two other dominant peaks are also observed from the base metal of the stainless steel substrate.

3.2. Electrochemical studies

The capacitance properties of the oxide electrodes were first evaluated by conducting cyclic voltammetry (CV) studies in 1.0 M aqueous solution of Li_2SO_4 within a potential window of −0.8 to 0 V. A comparison of the CV profiles obtained for the just annealed, and anodized (7 mA cm^{-2} for 30 min and 15 mA cm^{-2} for 15 min) samples is shown in Fig. 8. The CV tests were performed at a scan rate of 100 mV s^{-1} for all samples. A near rectangular CV response is obtained especially for the sample anodized at 15 mA cm^{-2} for 15 min. The capacitance behavior observed in this sample partly resembles to that of an electric double layer (EDL) capacitor with the CV current response close to rectangular shape having mirror image reflection about the zero-current line [36]. Moreover, the current responses in the CV scans at each reversal potential were also reasonably rapid [36]. The inset plot shows the comparison of the CV profiles for anodized (7 mA cm^{-2}) and the thermally oxidized samples. It can be observed that the enclosed areas under

these CV plots are rather small suggesting very low specific capacitance. This is expected based on the morphology of the oxide layers that formed on these samples. The layers were rather thin, compact, and dense, thereby restricting the efficient intercalation of the electrolyte with the oxide phase of the electrode material. Because of inefficient intercalation, the compact surface layers, as observed in these two conditions, restricts interfacial ions as well as charge transfer at the electrode/electrolyte interface [1]. Although the XRD profiles shows the formation of oxide layer in both samples (anodized at 7 mA cm^{-2} for 30 min and 15 mA cm^{-2} for 15 min) the difference in their capacitance behavior is primarily because of the morphology of the oxide layers in these two conditions. Owing to its thicker and porous morphology of the layer, it appears that the sample anodized for 15 min at 15 mA cm^{-2} resulted in much higher enclosed CV area suggesting enhanced specific capacitance (Fig. 3a). The nano-dendritic shape of the oxide layer produced cross linked multiporous structure enabling better charge and mass transfer through the diffusion of ions at the electrode/electrolyte interface. It has been reported that the layer architecture promoting effective electrode/electrolyte interaction in terms of mass and charge transfer are known to enhance capacitance performance of electrode material [37,38].

Fig. 9 presents the CV profiles for the samples anodized at 15 mA cm^{-2} for various periods of time (15−30 min). Apparently
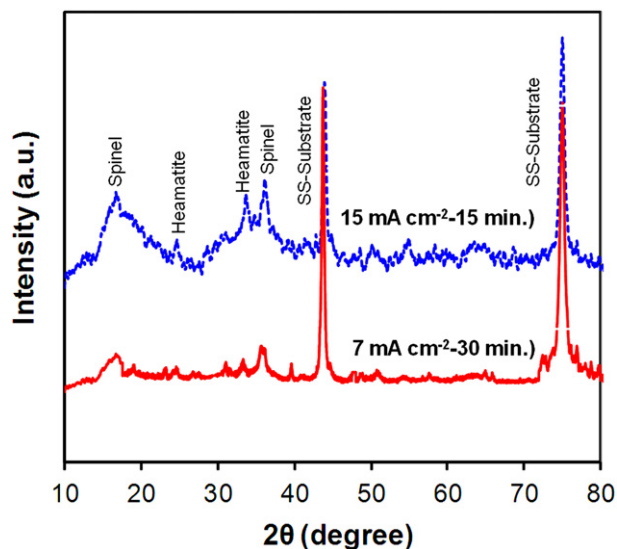
Fig. 7. XRD profile of the anodized stainless steel substrate at 7 mA cm^{-2} for 30 min and 15 mA cm^{-2} for 15 min.

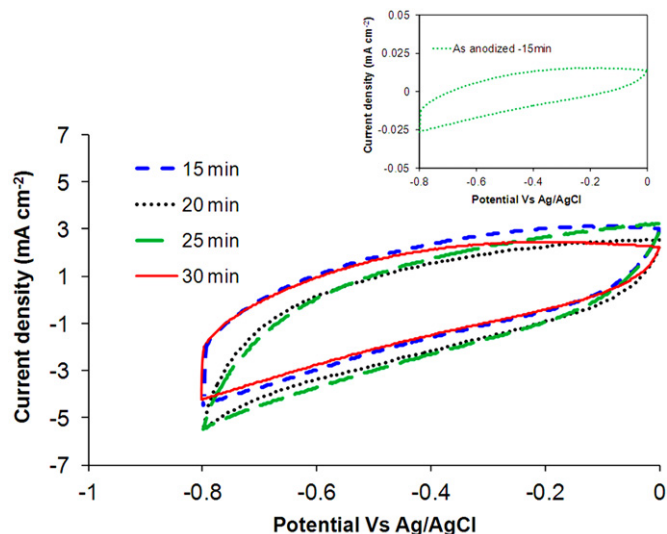Fig. 9. CV profiles of stainless steel samples anodized at 15 mA cm^{-2} for varied periods of times after annealing at 500 °C. The inset shows the CV profiles of the as-anodized sample prepared at 15 mA cm^{-2} for 15 min (without further anneal). Note that significantly less current values were obtained in the as-anodized condition.

the shape of the CV curves as well as the enclosed areas does not change significantly for these samples. Therefore, further increase in specific capacitance could not be achieved by increasing the anodization time although the thickness of the oxide layer increased up to ∼1.2 μm after 30 min of anodization. Furthermore, the porous morphology of the oxide layer was observed in all conditions, although the shape of the layer underwent transition from dendritic, foamy, rectangular, and spherical after 15, 20,25, and 30 min of anodization, respectively. It might be possible that porous oxide layer formed, irrespective of the anodization time, resulted in similar ionic conductivity and redox activity for all the samples leading to similar CV profiles. In order to establish the effect of annealing of the oxide layer on electrochemical properties, CV analysis was also performed on the as-anodized sample prepared at 15 mA cm^{-2} for 15 min. The CV profile is shown in the inset of Fig. 9. It can be noted that significantly decreased current

response was observed in the as-anodized condition. It may be partly due to the amorphous nature of the oxide layer in the as-anodized condition with reduced electrical conductivity [28].

Based on the forgoing discussions of the CV results, it appears that the nature/mechanism of the capacitance behavior observed in the stainless steel electrode is somewhat similar to that of the nanotubular oxide layer grown on pure iron [9]. However, the actual mechanism of charge–discharge and the nature of redox processes associated with iron oxide electrode itself is not very clear [39]. Several electrolytes such as Na$_2$SO$_3$ [40], Na$_2$SO$_4$ [38], Li$_2$SO$_4$ [9], KOH [38], NaOH [41], and NaCl [42] etc. have been used to evaluate the capacitance behavior of iron oxide electrodes prepared by various synthesis methods. In most of the studies, it was found that the capacitance of iron oxide was partly due to the ELD at the electrode/electrolyte interface and also through the charge storage by redox reactions on the surface of the host material [38,39]. In our case also, the primary contribution of the charge storage mechanism seems to be because of the EDL kind of behavior of the stainless steel oxide layer. However, the existence of some sort of redox process, especially due to the presence of the oxides of Cr and Ni in the spinel and hematite phases of the oxide layers, cannot be nullified.

The comparison of capacitance performance of the stainless steel electrode at various scan rates of the applied voltage was performed to evaluate the applicability of the material in high charging–discharging conditions. Generally, the specific capacitance of electrochemical capacitors decreases with increase in scan rate of the potential – the degree to which it will decrease depends on various factors such as the surface morphology and chemical composition of the electrode materials. Since, the CV responses for the samples anodized at 15 mA cm^{-2} for 15 min was similar to those samples prepared for higher time periods, most of the further studies were performed only in the former sample unless stated otherwise. The CV profiles, carried out at three different scan rates, 20, 100 and 200 mV s^{-1} are shown in Fig. 10(a). The near rectangular shape of the profile is maintained even at a higher scan rate (200 mV s^{-1}), indicating excellent capacitance behavior of the electrode. Based on the integrated area of the CV curves, the specific capacitance (C) were calculated using the following equation [40]
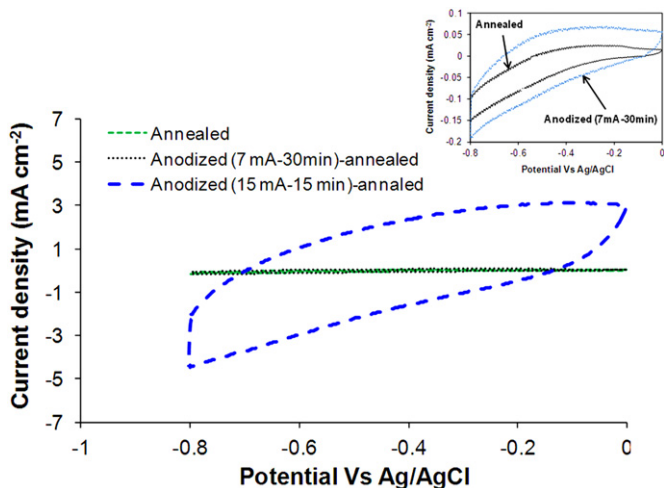

Fig. 8. CV profiles of stainless steel samples anodized at 7 mA cm^{-2} for 30 min and 15 mA cm^{-2} for 15 min after annealing at 500 °C. The inset shows the enlarged view of the CV profiles for the samples anodized at 7 mA cm^{-2} for 30 min and just annealed. The scan rate was fixed at 100 mV s^{-1}. The samples anodized at higher current density (15 mA cm^{-2} for 15 min) show larger CV areas demonstrating enhanced capacitance.

$$C = \frac{Q}{\Delta VA} \tag{1}$$

where, Q is the charge obtained from the integrated area of the CV, ΔV is the potential window, A is the active area of the electrode in contact with the electrolyte. The calculated specific capacitance values were 58, 42, and 32 mF cm^{-2} at the scan rates of 20, 100, and 200 mV s^{-1}, respectively. A 55% decrease in specific capacitance was observed when the scan rate was increased from 20 to 200 mV s^{-1}. To investigate the durability of the electrode, CV experiments were also carried out at 100 mV s^{-1} for up to 250 cycles. Fig. 10b shows the CV curves for the first and 250th cycles. Excellent cycle stability can be observed without any significant loss of conductivity even after 250th CV cycle.

The capacitance behavior of the porous stainless steel oxide electrode formed after 15 min of anodization at 15 mA cm^{-2} was also studied by galvanostatic charge–discharge experiments conducted at three different current densities: 1, 3, and 5 mA cm^{-2}. Fig. 11 shows the voltage–time (V–t) responses obtained at these current densities. The specific capacitance of the electrode at these current densities was calculated from the plots in Fig. 11 using the relationship:

$$C = \frac{It}{\Delta VA} \tag{2}$$

where, I represents the constant charge–discharge current density, t is the time form the V–t plots, ΔV is the voltage window, A is the area of the electrode. The calculated specific capacitance were 100, 49, and 25 mF cm^{-2} at current densities of 1,2, and 3 mA cm^{-2}, respectively. The inset in Fig. 9 shows the variation in specific capacitance with increase in current density. The specific capacitance decreased with increase in current density—a usual trend that occurs in supercapacitors [40].

The stability of the electrode was also examined by employing continuous charge–discharge cycle up to a total number of 500 cycles. The V–t profiles obtained at a current density of 1 mA cm^{-2} of the charge–discharge cycles are shown in Fig. 12. Fig. 12(a,b,c) illustrates a few of the representative V–t curves obtained at the beginning, middle and toward the end of the cycle periods, respectively. These experimental data demonstrates that a fairly stable capacitance behavior can be achieved even after 500 cycles of charge–discharge. This result also validates the finding of the stable CV response obtained on this electrode after 250 cycles (Fig. 10b). Variations in slopes of the V–t curves were observed,
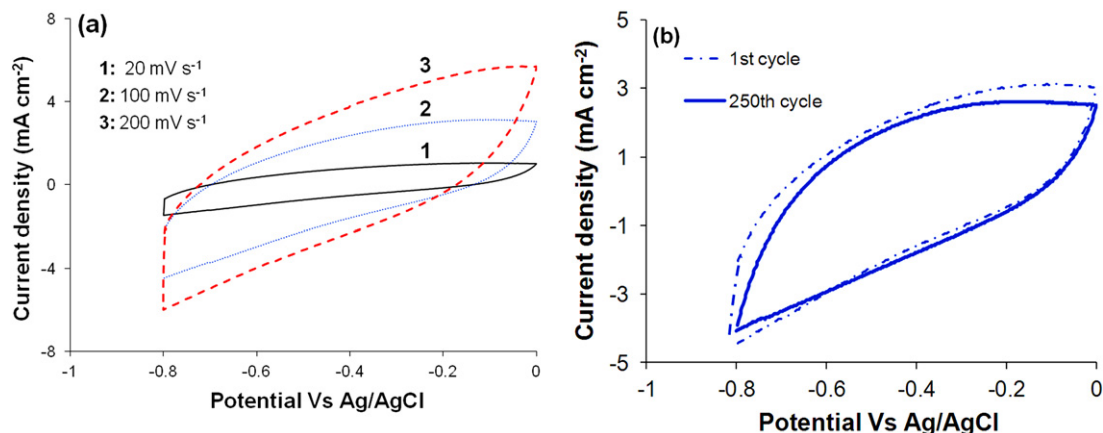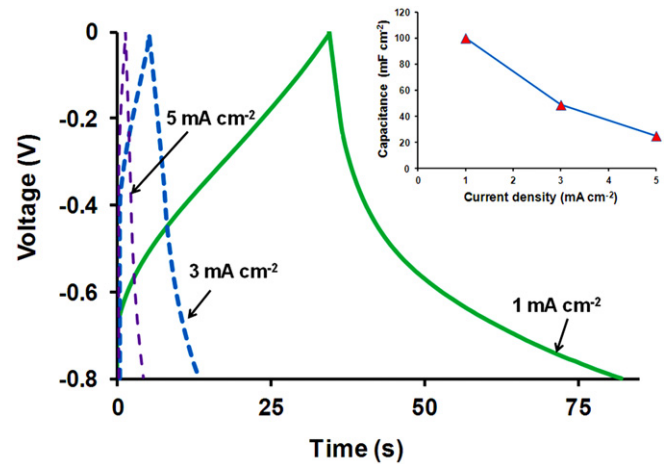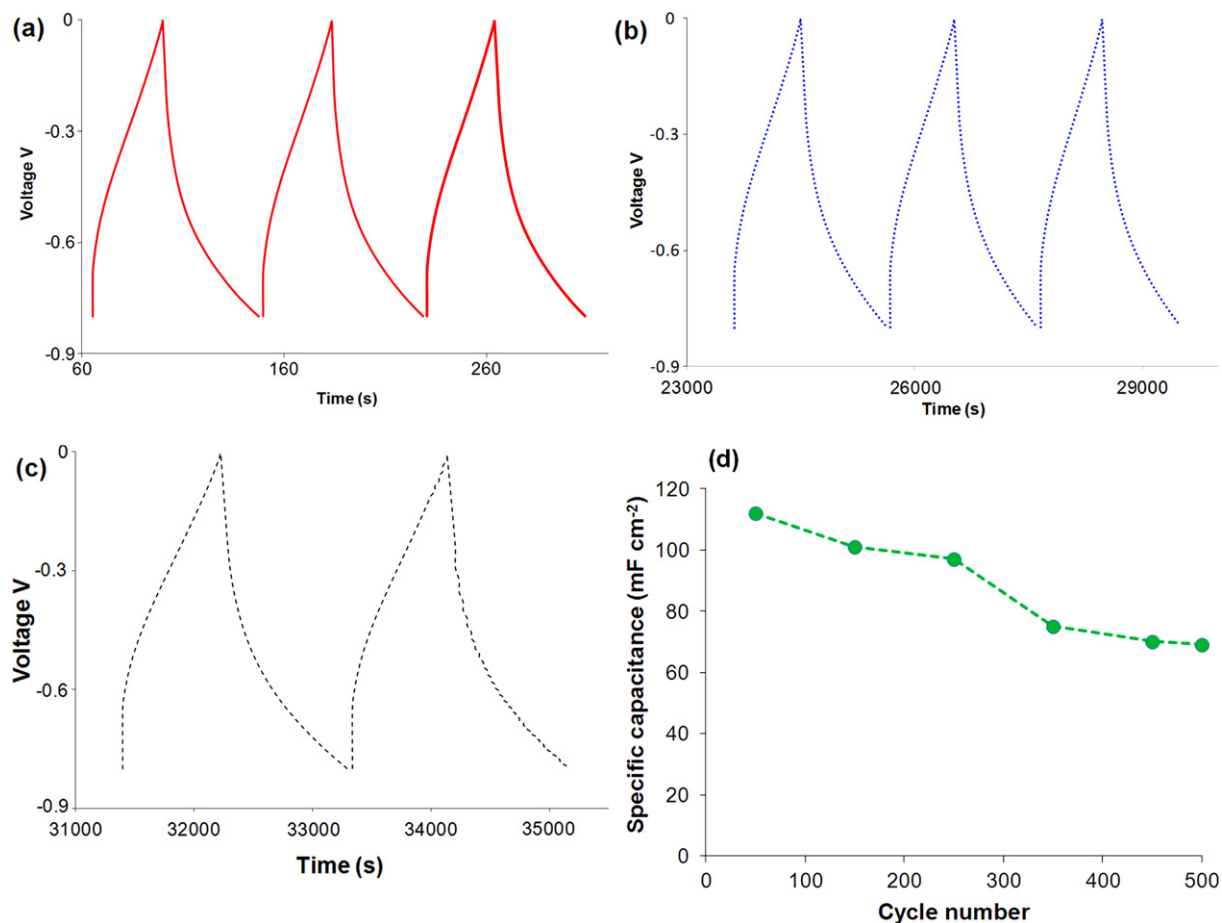

Fig. 11. Galvanostatic charge–discharge plots of anodized stainless steel (15 mA cm^{-2} for 15 min) sample at various current densities. (The inset figure shows the variation of specific capacitance as the function of current densities). Note that the specific capacitance decreases with increase in charge–discharge current density.

which is a typical indication of some sort of pseudocapacitance nature of the electrode/electrolyte system. Possible electrochemical redox reaction might have occurred on the surface of the stainless steel electrode in presence of the electrolyte. The specific capacitance (calculated using Eq. (2)) exhibited by the electrode at the beginning of the cycling (Fig. 12a) is about 112 mF cm^{-2}, which gradually decreased to about 70 mF cm^{-2} after 500 cycles (Fig. 12c). Fig. 12d shows the variations in the specific capacitance at regular intervals throughout the entire charge–discharge period. The capacitance retention of the stainless steel electrode was about 62% after 500 cycles, demonstrating good electrochemical stability of the electrode material.

To study further the capacitance and electronic properties of the oxide layers, electrochemical impedance spectroscopic (EIS) experiments were conducted. Fig. 13 shows the Nyquist plots for stainless steel samples galvanostatically anodized at 7 mA cm^{-2} for 30 min and at 15 mA cm^{-2} for 15 and 30 min. The impedance plots, obtained in these samples, can be divided in to low and high frequency regions. In the high frequency regions, devoid of partial semicircular profiles, generally observed in many other oxide supercapacitors [43,44], indicated that no charge transfer limiting process had occurred that usually results from a parallel

Fig. 10. (a) CV profiles of the anodized stainless steel (15 mA cm^{-2} for 15 min) sample at various scan rates. (b) The 1st and 250th CV profiles of the anodized stainless steel (15 mA cm^{-2} for 15 min) sample at a scan rate of 100 mV s^{-1}. Excellent capacitance retention even after 250th CV cycle.

Fig. 12. Compilations of *V–t* responses of anodized stainless steel (15 mA cm⁻² for 15 min) sample at (a) beginning, (b) middle, (c) end of a 500 charge–discharge operation at 1 mA cm⁻². (d) Variations in specific capacitance as the function of cycle number.

combination of internal resistance and capacitance [45]. In this region, the plot shows a linear, straight line relationship for all samples suggesting good charge transfer behavior with low electrical resistivity. The diffuse resistance (characterize by the Warburg impedance, W) of the electrolyte in to the pores of the electrode materials can be analyzed by examining the Nyquist plots at the low frequency regions. The low frequency profile for the sample anodized at 7 mA cm⁻² for 30 min shows near 45° slope with respect to the real and imaginary axes. Similar response was also observed in the case of pure titania nanotube electrode [1]. The authors believed that the reason for such trend was the semi infinite ion diffusion of the electrolyte in to the oxide electrode. However, for the stainless steel electrodes anodized at 15 mA cm⁻² for 15 and 30 min, considerable deviations from the imaginary axis can be observed. This result can be explained based on the enhanced redox activity associated with these two sample conditions. Generally, in case of electrodes exhibiting EDL type capacitance behavior, the low frequency curve shows a near vertical trend along the imaginary axis. In case of pseudocapacitor with redox process occurring in the electrode/electrolyte interface, the EIS profile deviates from the imaginary axis and tend to lie along the real axis. Therefore, higher redox induced capacitance can be observed for the samples anodized at 15 mA cm⁻² compared to the samples anodized at 7 mA cm⁻². This is in accordance to the CV results obtained in these samples (Fig. 8). Further, the capacitance behavior for the samples anodized for 15 and 30 min at 15 mA cm⁻² should be similar to each other based on the low and high frequency EIS data obtained in these samples. The prior discussions on the CV results obtained for

these samples also comply with this observation (Figs. 8 and 9). Therefore, these consistent and remarkable data truly suggest that low charge transfer resistance and high capacitance can be achieved in the oxide layer grown on stainless steel substrate.
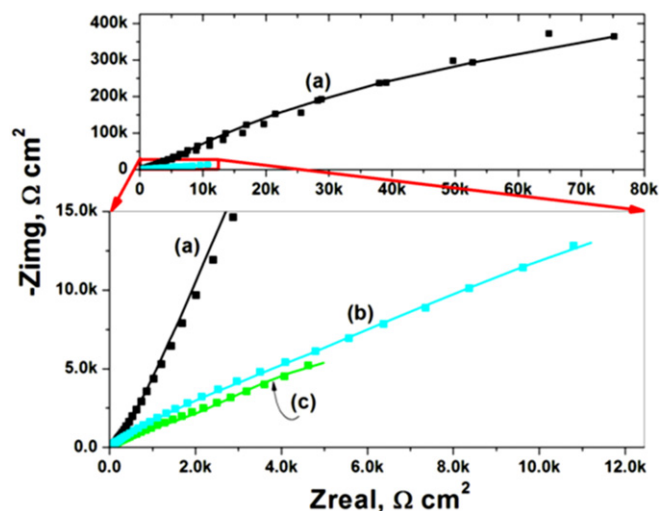
Fig. 13. Nyquist plot of (a) anodized stainless steel at 7 mA cm⁻² for 30 min, (b) 15 mA cm⁻² for 15 min, and (c) 15 mA cm⁻² for 30 min. Impedance analysis was carried out over the frequency range of 0.01–10,000 Hz in 1 M Li₂SO₄ at open-circuit potential conditions with an applied AC potential of 10 mV.

4. Conclusions

The following conclusion can be drawn from this study:

1. Galvanostatic anodization of 302 type stainless steel in a fluorinated ethylene glycol solution resulted in the formation of oxide layers. Depending on the current densities employed during anodization, various morphologies of the oxide layer could be obtained.
2. At a lower current density of anodization (7 mA cm^{-2}), a thin (~300 nm) and compact oxide layer was formed which was similar in morphology to that of the oxide layer formed by just annealing at 500 °C for 2 h. However, when anodization was carried out at 15 mA cm^{-2}, the shape of the layer underwent transition from dendritic, foamy, rectangular, and spherical shapes after 15, 20, 25, and 30 min anodization, respectively. Further, the thickness of the oxide layer grew thicker, resulting in 0.7 and 1.2 μm in lengths after 15 and 30 min, respectively. The morphology of the oxide layer obtained after 15 min was nano-dendritic (~50 nm in width, ~150–200 nm in length), while after 30 min, it became spherical ($d \sim$ 150–350 nm).
3. The X-ray diffraction performed on the anodized oxide layers suggested the formation of hematite (($Fe, Cr)_2O_3$) and spinel (($Ni, Cr, Fe)_3O_4$) phases.
4. The electrochemical capacitance performance of the electrode material was studied in 1 M Li_2SO_4 solution in a potential window of 0 to −0.8 V. The CV, galvanostatic charge–discharge experiments indicated excellent stability and reversibility of the stainless steel electrode material. The capacitance behavior was due to both EDL as well as pseudocapacitance nature of the electrode. It was found that more than 60% of the capacitance was retained even after 500 cycles of continuous charge–discharge cycles suggesting the stainless steel electrode as an excellent material to be used in supercapacitor applications.
5. The EIS study performed on the oxide layers formed at the anodization current density of 7 mA cm^{-2} for 30 min showed relatively higher charge transfer resistance and lower redox induced capacitance behavior compared to those anodized at 15 mA cm^{-2}. Furthermore, similar charge transfer and redox behavior was predicted from the EIS data for the samples anodized for 15 and 30 min at 15 mA cm^{-2}. These results are consistent with the CV performance as well as the morphology of the oxide later formed after anodization at different conditions.

Acknowledgment

References

[1] Y. Xie, L. Zhou, C. Huang, H. Huang, J. Lu, Electrochim. Acta 53 (2008) 3643–3649.
[2] Z. Yang, C.-Y. Chen, H.-T. Chang, J. Power Sources 196 (2011) 7874–7877.
[3] D. Pech, M. Brunet, H. Durou, P. Huang, V. Mochalin, Y. Gogotsi, P.-L. Taberna, P. Simon, Nat. Nanotechnol. 5 (2010) 651–654.
[4] C.-M. Chuang, C.-W. Huang, H. Teng, J.-M. Ting, J. Electrochem. Soc. 157 (2010) K113–K117.
[5] P. Simon, Y. Gogotsi, Nat. Mater. 7 (2008) 845–854.
[6] B. Babakhani, D.G. Ivey, J. Power Sources 195 (2010) 2110–2117.
[7] M. Hasan, M. Jamal, K.M. Razeeb, Electrochim. Acta 60 (2012) 193–200.
[8] J. Xu, L. Gao, J. Cao, W. Wang, Z. Chen, Electrochim. Acta 56 (2010) 732–736.
[9] K. Xie, J. Li, Y. Lai, W. Lu, Z. Zhang, Y. Liu, L. Zhou, H. Huang, Electrochem. Commun. 13 (2011) 657–660.
[10] M.-S. Wu, R.-H. Lee, J. Electrochem. Soc. 156 (2009) A737–743.
[11] R.R. Rangaraju, K.S. Raja, A. Panday, M. Misra, Electrochim. Acta 55 (2010) 785–793.
[12] S.P. Albu, A. Ghicov, P. Schmuki, Phys. Status Solidi RRL 3 (2009) 64–66.
[13] S.K. Mohapatra, S.E. John, S. Banerjee, M. Misra, Chem. Mater. 21 (2009) 3048–3055.
[14] R.R. Rangaraju, A. Panday, K.S. Raja, M. Misra, J. Phys. D: Appl. Phys. 42 (2009) 135303.
[15] M. Misra, K.S. Raja, in: L. Vayssieres (Ed.), On Solar Hydrogen & Nanotechnology, John Wiley & Sons, Chichester, UK., 2010.
[16] H. Masuda, K. Fukuda, Science 268 (1995) 1466.
[17] V. Zwilling, M. Aucouturier, E. Darque-Ceretti, Electrochim. Acta 45 (1999) 921.
[18] W.J. Lee, W.H. Smyrl, Electrochem. Solid-State Lett. 8 (2005) B7.
[19] H. Tsuchiya, P. Schmuki, Electrochem. Commun. 7 (2005) 49.
[20] A. Norlin, J. Pan, C. Leygraf, J. Electrochem. Soc. 153 (2006) B225.
[21] K.S. Raja, M. Misra, K. Paramguru, Electrochim. Acta 51 (2005) 154–165.
[22] Y.R. Smith, B. Sarma, S.K. Mohanty, M. Misra, Int. J. Hydrogen Energy 38 (2013) 2062–2069.
[23] P. Roy, S. Berger, P. Schmuki, Angew. Chem. 50 (2011) 2904–2939.
[24] B. Sarma, Y.R. Smith, S.K. Mohanty, M. Misra, Mater. Lett. 85 (2012) 33–36.
[25] Y.R. Smith, B. Sarma, S.K. Mohanty, M. Misra, Electrochem. Commun. 19 (2012) 131–134.
[26] Y.R. Smith, B. Sarma, S.K. Mohanty, M. Misra, ACS Appl. Mater. Interfaces 4 (2012) 5883–5890.
[27] F. Martin, D.D. Frari, J. Cousty, C. Bataillon, Electrochim. Acta 54 (2009) 3086–3091.
[28] K. Kure, Y. Konno, E. Tsuji, P. Skeldon, G.E. Thompson, H. Habazaki, Electrochem. Commun. 21 (2012) 1–4.
[29] H. Tsuchiya, T. Suzumura, Y. Terada, S. Fujimoto, Electrochim. Acta 82 (2012) 333–338.
[30] G. Lota, E. Frackowiak, J. Mittal, M. Monthioux, Chem. Phys. Lett. 434 (2007) 73–77.
[31] N.K. Shrestha, S.J. Yoon, M. Lee, D.Y. Lee, I. Lim, R.S. Mane, M.M. Sung, S.-H. Han, Microporous Mesoporous Mater. 144 (2011) 200–204.
[32] M. Sun, X. Wu, Z. Zhang, E. Han, Corros. Sci. 51 (2009) 1069–1072.
[33] N.E. Hakiki, M.F. Montemor, M.G.S. Ferreira, M.C. Belo, Corros. Sci. 42 (2000) 687–702.
[34] W. Kuang, E. Han, X. Wu, J. Rao, Corros. Sci. 52 (2010) 3654–3660.
[35] M. Sun, X. Wu, E. Han, J. Rao, Scr. Mater. 61 (2009) 996–999.
[36] B.E. Conway, J. Electrochem. Soc. 138 (1991) 1539.
[37] W. Xing, F. Li, Z.F. Yan, G.Q. Lu, J. Power Sources 134 (2004) 324.
[38] K. Jurewicz, C. Vix-Guterl, E. Frackowiak, S. Saadallah, A. Reda, J. Parmentier, J. Patarin, F. Beguin, J. Phys. Chem. Solids 65 (2004) 287.
[39] T. Cottineau, M. Toupin, T. Delahaye, T. Brousse, D. Belanger, Appl. Phys. A: Mater. Sci. Process. 82 (2006) 599.
[40] S.Y. Wang, K.C. Ho, S.L. Kuo, N.L. Wu, J. Elelectrochem. Soc. 153 (2006) A75.
[41] P.M. Kulal, D.P. Dulal, C.D. Lokhande, V.L. Fulari, J. Alloys Compd. 509 (2011) 2567–2571.
[42] N.L. Wu, S.Y. Wang, C.Y. Han, D.S. Wu, L.R. Shiue, J. Power Sources 113 (2003) 173–178.
[43] S.-J. Bao, C.M. Li, C.-X. Guo, Y. Qiao, J. Power Sources 180 (2008) 676–681.
[44] B.-X. Zou, Y. Liang, X.-X. Liu, D. Diamond, K.-T. Lau, J. Power Sources 196 (2011) 4842–4848.
[45] M. Salari, K. Konstantin, H.K. Liu, J. Mater. Chem. 21 (2011) 5128–5133.